

Robotic Manipulation of Deformable Cells for Orientation Control

Changsheng Dai , Zhuoran Zhang , Yuchen Lu, Guanqiao Shan , Xian Wang , Qili Zhao, Changhai Ru, and Yu Sun , *Fellow, IEEE*

Abstract—Robotic manipulation of deformable objects has been a classic topic in robotics. Compared to synthetic deformable objects such as rubber balls and clothes, biological cells are highly deformable and more prone to damage. This article presents robotic manipulation of deformable cells for orientation control (both out-of-plane and in-plane), which is required in both clinical (e.g., *in vitro* fertilization) and biomedical (e.g., clone) applications. Compared to manual cell orientation control based on empirical experience, the robotic approach, based on modeling and path planning, effectively rotates a cell, while consistently maintaining minimal cell deformation to avoid cell damage. A force model is established to determine the minimal force applied by the micropipette to rotate a spherical or, more generally, ellipsoidal oocyte. The force information is translated into indentation through a contact mechanics model, and the manipulation path of the micropipette is formed by connecting the indentation positions on the oocyte. An optimal controller is designed to compensate for the variations of

mechanical properties across oocytes. The polar body of an oocyte is detected by deep neural networks with robustness to shape and size differences. In experiments, the system achieved an accuracy of 97.6% in polar body detection and an accuracy of 0.7° in oocyte orientation control with maximum oocyte deformation of 2.70 μm throughout the orientation control process.

Index Terms—Cell manipulation, deformable object manipulation, deformation, force, orientation control.

I. INTRODUCTION

ROBOTIC manipulation of deformable objects has wide applications in industrial [1], healthcare [2], and clinical [3] settings. Compared to the manipulation of rigid objects, path planning for deformable object manipulation is more challenging, since the object changes its shape under an applied force. Thus, the object's deformation behavior must be accurately modeled when designing the manipulation path [4].

Biological cells represent a class of deformable objects that are delicate and highly deformable. The deformation of cells in robotic cell manipulation (e.g., transportation [5], characterization [6], and surgery [7]) must be minimized to avoid cell damage. In cell surgery tasks, such as in intracytoplasmic sperm injection [8], embryo biopsy [9], pronuclear transfer [10], and cell transfection [11], cell orientation control is a crucial procedure. For instance, in mammalian oocyte manipulation, the polar body of the oocyte must be rotated away from the injection site [3 o'clock, Fig. 1(a) and (b)] to prevent damage to the spindle, which is in the proximity of the polar body inside the oocyte. The accuracy of orienting the polar body is important for achieving a high fertilization rate and preserving embryo development potential [12].

Cell rotation was attempted using fluid flow induced by pressure [13] or vibration [14]; however, the orientation control accuracy is susceptible to flow inertia and the cell position in the fluid flow field. Optical tweezers used a focused laser beam to apply forces on a cell for rotation [15], but may risk photodamage to the cell [16]. Orientation control leveraging dielectrophoretic forces was also demonstrated, but the effect of the applied electrical field on cell development is unknown [17]. Microscope rotational stages [18], mechanical devices [19], and magnetic microrobots [20] were also developed for cell orientation control. However, these methods require additional devices and hardware, which alter the standard setup and disrupt the standard workflow used in clinics and biomedical labs.

Manuscript received July 21, 2019; accepted October 2, 2019. This paper was recommended for publication by Associate Editor C. Bergeles and Editor P. Dupont upon evaluation of the reviewers' comments. This work was supported in part by the Natural Sciences and Engineering Research Council of Canada and in part by the Canada Research Chairs Program. (*Corresponding author: Yu Sun.*)

C. Dai, Z. Zhang, G. Shan, X. Wang, and Y. Sun are with Advanced Micro and Nanosystems Laboratory, University of Toronto, Toronto, ON M5S 3G8, Canada (e-mail: changsheng.dai@mail.utoronto.ca; zhuoran@mie.utoronto.ca; gq.shan@mail.utoronto.ca; wangxiantju@hotmail.com; sun@mie.utoronto.ca).

Y. Lu was with the Advanced Micro and Nanosystems Laboratory, University of Toronto, Toronto, ON M5S 3G8, Canada. He is now with the University of California, San Diego, La Jolla, CA 92093 USA (e-mail: yuchen.lu@mail.utoronto.ca).

Q. Zhao was with the Advanced Micro and Nanosystems Laboratory, University of Toronto, Toronto, ON M5S 3G8, Canada. He is now with Nankai University, Tianjin 300350, China (e-mail: zhaqili19860106@163.com).

C. Ru is with Research Center of Robotics and Micro System and the Collaborative Innovation Center of Suzhou Nano Science and Technology, Soochow University, Suzhou 215021, China (e-mail: rchhai@hotmail.com).

This article has supplementary downloadable material available at <http://ieeexplore.ieee.org>, provided by the authors. The material consists of a video, viewable with any version of Windows Media Player or a player that supports basic MP4 file, showing robotic manipulation of deformable cells for orientation control (both out-of-plane and in-plane). Compared to manual cell rotation control based on empirical experience, the robotic approach, based on mathematical modeling and path planning, effectively rotates a cell while consistently maintaining minimal cell deformation to avoid cell damage. An optimal controller is designed to compensate for the variations of mechanical properties across cells. The polar body of an oocyte is detected by deep neural networks with robustness to shape and size differences. The video shows that to rotate the polar body to target orientation, manual orientation control suffered from large cell deformation. The developed robotic orientation control can rotate an ellipsoidal oocyte with minimal cell deformation, thus reducing potential cell damage. Contact Yu Sun (e-mail: sun@mie.utoronto.ca) for further questions about this work.

Color versions of one or more of the figures in this article are available online at <http://ieeexplore.ieee.org>.

Digital Object Identifier 10.1109/TRO.2019.2946746

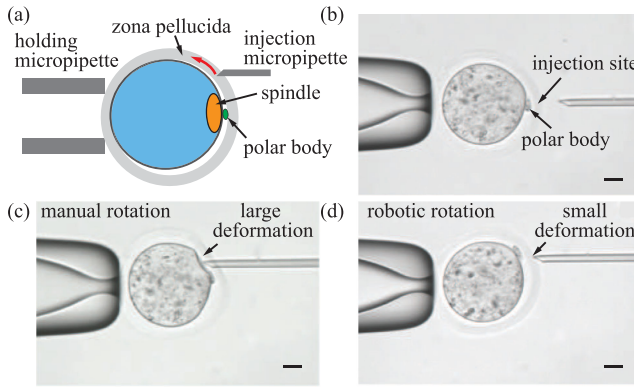


Fig. 1. (a) and (b) Polar body in the mammalian oocyte must be rotated away from the 3 o'clock position (i.e., injection site) toward the 6 or 12 o'clock position to protect the spindle, which is close to the polar body inside the oocyte. In a standard clinical setup, the oocyte is held by a holding micropipette. When the injection micropipette is controlled to push the oocyte, the friction force between the injection micropipette and the zona pellucida (oocyte's outer membrane) causes the oocyte to rotate. (c) In manual rotation, oocyte damage can arise from undesired large deformations. (d) Robotic orientation control reported in this article achieves oocyte rotation with minimal oocyte deformation. Scale bar: 10 μm .

Presently, in clinical and biomedical lab operation, manual oocyte orientation control is performed using a holding micropipette to gently hold the oocyte and an injection micropipette to push the oocyte and empirically rotate it. This approach is deterministic for controlling the orientation of the oocyte because the oocyte follows the movement of the injection micropipette due to the friction force between them. However, it is difficult to control oocyte deformation during manual rotation [see Fig. 1(c)].

Compared to synthetic deformable objects, cells are more fragile and prone to damage under large deformation [21]. Take mammalian oocytes as an example. Large deformation of oocytes can cause spindle damage and lead to development failure [22]. Large deformation can also increase the internal pressure of the oocyte and contribute to oocyte degeneration. With smaller oocyte/embryo deformation, both the oocyte fertilization rate and the embryo development rate have been shown to be significantly higher [23], [24]. This article aims to develop a robotic orientation control approach to achieve a high accuracy and minimal cell deformation throughout the cell rotation process.

To model an object's deformations during robotic manipulation, the mass-spring-damper model is straightforward to implement but provides limited accuracy [25]. In contrast, finite-element modeling provides higher accuracy but has a high computation cost [26]. Model parameters can be attained from prior knowledge [27] or estimated by calibration prior to manipulation [25]. Manipulation without prior knowledge or calibration can be implemented via visual servoing [28], [29], in which the deformation Jacobian matrix is estimated online to relate the movement of the manipulator to the movement of selected deformation feature points on the deformable object.

To design the manipulation path for deformable objects, several path planning methods have been reported, including probabilistic roadmap [30] and minimal energy optimization [31].

These existing path planning methods were developed to achieve desired deformation of the manipulated object with designed motion paths. Differently, the aim of this article is to achieve desired motion (i.e., cell rotation) with designed cell deformation. The designed deformation must be minimized to reduce cell damage during manipulation.

To control the force applied to a cell, force sensors were developed for sensing cellular forces, and force sensing was incorporated into robotic manipulation for hybrid force/position control [32] or impedance control [33]. However, practical integration difficulties, such as gluing and meticulous alignment, prevent them from being incorporated into standard setups commonly used in clinical and biomedical labs, which utilize glass micropipettes (see Fig. 1) and pure visual feedback for cell manipulation.

The challenges to overcome, in this article, are as follows.

- 1) The polar body has low contrast in microscopy imaging and has irregular shape [34], posing difficulties to polar body detection.
- 2) Oocyte deformation must be constrained when controlling the injection micropipette to push the oocyte for rotating the oocyte.
- 3) Oocytes have different ellipticity in shape [35], Young's modulus, and friction coefficients, which must be taken into account for orientation control.

We tackled these problems by using deep neural networks (DNNs) for robust polar body detection, force modeling and path planning for orientation control with minimal oocyte deformation, and optimal control to accommodate oocytes' mechanical variations. Experimental results demonstrate that the system achieved an accuracy of 97.6% in polar body detection and an accuracy of 0.7° in oocyte orientation control with cell deformation smaller than $2.70 \mu\text{m}$. The time cost for cell orientation control was 10–15 s, comparable to that of manual operation by an experienced operator.

The major difference between existing approaches and our technique is our use of unfixed constraint in manipulation, as inherently required for cell orientation control. Fixed constraints (i.e., no relative movement) are commonly applied between the robotic manipulator and the object, for tasks such as grasping [26], knotting [36], and suturing [3]. An unfixed constraint is used in our orientation control, which permits relative movement between the manipulator and the object. For orientation control, robotic manipulators equipped with revolute joints can easily control the pose (e.g., orientation) of a deformable object; however, robotic micromanipulators typically have no rotational degrees of freedom (DOF). Because microscopes have a limited field of view and depth of field, rotation-induced translation easily causes the micromanipulator and end-tool to move out of the field of view and focus [37]. To control the manipulated object's rotational DOF, the unfixed constraint is incorporated in our force modeling and path planning. The technique reported in this article can be generally applicable to manipulating deformable objects (not limited to cells) with unfixed constraints while achieving minimal deformation.

Compared to its conference version [38], this article contains significantly more technical details, in particular on polar body

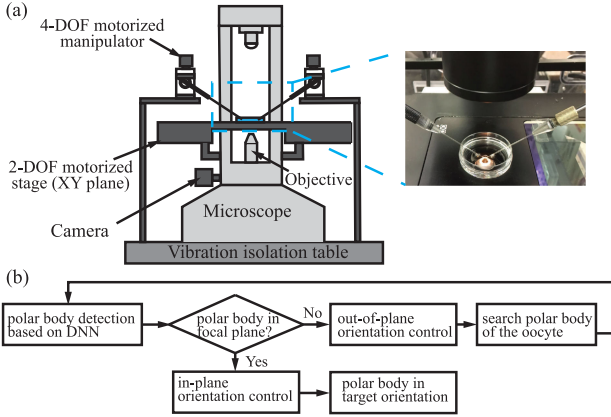


Fig. 2. (a) System setup used in this article is identical to the standard configuration used in clinics and biomedical labs. Two glass micropipettes are mounted on two robotic manipulators for achieving cell manipulation tasks. (b) Operation sequence. If the polar body is not detected, out-of-plane orientation control is performed to search for the polar body and rotate it into the focal plane. Then, in-plane orientation control is performed to rotate the polar body to target orientation.

detection and orientation modeling. In addition, our previous work reported in the conference paper used a proportional–integral (PI) controller to reduce the orientation error caused by variations in mechanical parameters across cells, where the control gains were experimentally tuned. Although the PI controller helped reduce orientation errors, it caused relatively large indentation (deformation) on the cell, since the controller had no constraint on cell deformation. In this article, an optimal controller is designed for cell orientation control, and a cost function is formulated. The control gains are derived by minimizing the cost function that incorporates both orientation error and cell deformation. Experiments were designed to compare the performance between the optimal controller and the proportional–integral–derivative (PID) controller, and optimal controller achieved significantly less cell deformation than the PID controller.

II. ROBOTIC SYSTEM FOR CELL ORIENTATION CONTROL

A. Standard Clinical Setup

As shown in Fig. 2(a), the system consists of an inverted microscope equipped with an XY motorized stage (H117, Prior). A clinical-use injection micropipette (MIC-50-35, Origio) and a holding micropipette (MPH-SM-35, Origio) were mounted on two 4-DOF micromanipulators (MX7600, Siskiyou) with a motion resolution of $0.1 \mu\text{m}$. The holding micropipette was connected with a pneumatic pump for oocyte aspiration. A camera (scA1300-32gm, Basler) was connected to the microscope to capture images at 30 frames/s. The inset in Fig. 2(a) shows a Petri dish placed on the heating plate (on the XY stage) for 37°C temperature control.

The operation sequence of robotic orientation control is summarized in Fig. 2(b). The position of the polar body is detected by DNNs. If the polar body is not detected in the focal plane, the system performs out-of-plane orientation control to search for

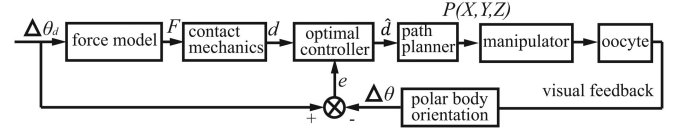


Fig. 3. Path planning for orientation control of deformable oocytes. For each orientation step $\Delta\theta_d$, a force model is used to determine the required minimal force F to rotate the oocyte. The force is translated into injection micropipette’s indentation d on the oocyte by contact mechanics. An optimal controller is designed to compensate for the variations of oocytes’ mechanical parameters. The optimal controller updates the indentation to \hat{d} based on the error e between the expected orientation increment $\Delta\theta_d$ and the measured orientation increment $\Delta\theta$ from visual feedback. The objective of the optimal controller is to minimize the orientation error and oocyte deformation. The manipulation path is formed by connecting the indentation positions P of the injection micropipette.

the polar body and rotate it into the focal plane. Then, in-plane orientation control is performed to rotate the polar body to the target orientation.

B. Problem Formulation

Mammalian oocytes are highly deformable. Robotic orientation control of an oocyte requires path planning of the injection micropipette. The path for rotating the oocyte is divided into multiple steps, each corresponding to an indentation position of the injection micropipette. The path is designed to rotate an oocyte with minimal oocyte deformation, thus reducing oocyte damage. This orientation control problem is recapitulated as a constrained optimization problem, i.e., the total deformation D of the oocyte during orientation control is minimized under the constraint that the oocyte is rotated to the desired orientation θ_d . The objective function is

$$\min D = \sum_i d_i \text{ subject to } \theta_d = \sum_i \Delta\theta_i \quad (1)$$

where d_i is the micropipette indentation depth at orientation step i , and $\Delta\theta_i$ is the orientation increment of the oocyte at orientation step i . This constrained optimization problem is solved using optimal control, as described in Section V.

The process of path planning is shown in Fig. 3. The unfixed constraint between the oocyte and the holding micropipette is included in the force modeling and path planning. For each orientation step (control cycle) $\Delta\theta_d$, a force model determines the required minimal force F to apply to the oocyte. The force is then translated into the micropipette indentation d on the oocyte by contact mechanics. The indentation is updated to \hat{d} by the optimal controller based on the orientation error e . The manipulation path is planned by connecting the indentation positions P of the micropipette in each orientation step.

Oocytes’ geometrical and mechanical properties must be taken into account in path planning. The contour of an oocyte’s zona pellucida (outer membrane of the oocyte) is detected by thresholding the local standard deviations of the image. Local standard deviations are used to increase the contrast of the image. An ellipse is then least squares fitted using the zona pellucida’s contour. In force analysis, an ellipsoidal oocyte model is established from the fitted ellipse to accommodate shape differences among oocytes.

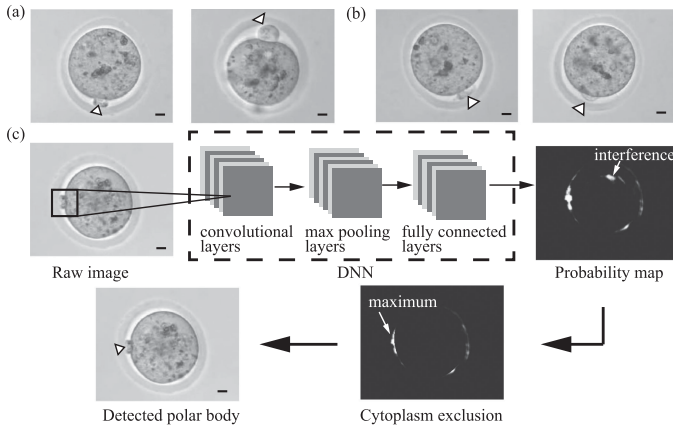


Fig. 4. (a) Shape and size of polar bodies vary among different oocytes. (b) Shape and focus of the same polar body change significantly when the oocyte is rotated. Polar body is labeled with triangles. (c) Polar body detection by DNNs. The networks are composed of convolutional, max pooling, and fully connected layers. The output of the networks is a probability map showing the presence possibility of the polar body. To prevent interference from the cytoplasm (arrow labeled), a circular region is determined around the centroid of the cytoplasm and is excluded for polar body detection. By finding the maximum in the probability map, the position of the polar body (triangle labeled) is determined. Scale bar: $10 \mu\text{m}$.

Oocytes also have different Young's modulus values and friction coefficients with micropipettes. The variations of mechanical parameters can cause the force applied by the injection micropipette to be insufficient for rotating the oocyte. Although Young's modulus and friction coefficient can be experimentally calibrated [39], [40], both calibration procedures are time consuming (e.g., 5 min for measuring Young's modulus using micropipette aspiration). The incubator has a temperature of 37°C and a CO_2 concentration of 5%. Temperature fluctuation can cause spindle disassembly [41], and CO_2 variation affects pH of culture media and lowers cell development potential [42]. Thus, it is desired to minimize the time cost of each cell manipulation procedures. In this article, an optimal controller (see Fig. 3) is designed to compensate for the variations of oocytes' mechanical parameters without conducting the lengthy calibrations. The optimal controller updates the indentation to minimize the orientation error caused by the oocyte variations and to minimize the oocyte deformation.

III. POLAR BODY DETECTION

The detection of the polar body is necessary for the system to determine the orientation of the polar body and to design the manipulation path for orientation control. Existing methods for polar body detection rely on edge detection [43] and image thresholding [13], which involve manually selected features. When the objects to detect have large variations in selected features, detection accuracy of these methods is often compromised [44]. Since the shape and size of the polar body vary significantly among different oocytes [e.g., the two oocytes shown in Fig. 4(a)], and the shape and focus of the same polar body also change when the oocyte is rotated [see Fig. 4(b)], existing methods are not effective for accommodating variations in shape, size, and focus of the polar body.

In this article, DNNs are used to robustly detect the polar body. DNNs have been widely applied to image analysis [44], since it is capable of automatically learning visual features for classification. It was shown to outperform traditional methods (e.g., thresholding and edge detection) for the detection of microglial cells [45] and cell nucleus [46]. Training the DNN with images that contain polar bodies of different sizes, shapes, and focus, the DNN can robustly detect polar bodies with these variations. As shown in Fig. 4(c), the networks start with convolutional layers, which perform convolution on the input images with a rectangular filter. They are followed by max pooling layers to subsample the previous layer by combining a cluster of neurons into a single one. The last three layers are fully connected layers, which connect neurons with every neuron in the previous layer. Adaptive moment estimation is used to optimize the network weights.

In an input image, the pixel at the center of the polar body was manually labeled as 1, while other pixels were labeled as 0. The training set consists of square patches of the input images labeled as the same class as their central pixels. One apparent problem of the training set was the unbalanced class distribution, i.e., in an image of 1200×900 pixels, only one pixel was labeled as 1. Thus, the trained networks would be biased toward Class 0, but finding Class 1 (polar body) should be the goal of the networks. Therefore, data balancing was performed to keep a balanced distribution between classes. First, the neighboring pixels were also labeled as 1 if closer than two pixels to the manually labeled center of the polar body. The image patches labeled as 1 were rotated to have more image patches in different orientations. To reduce the number of image patches in Class 0, the image patches with intensity variances below a preset threshold were excluded from the training set. As shown in Fig. 1(b), most of the regions with low intensity variances are the background without the cell and micropipettes; hence, removing them from the training set did not affect the learning of image features.

Another difficulty for DNN-based polar body detection was the interference from the cytoplasm inside an oocyte. The cytoplasm has similar color and texture to the polar body [e.g., Fig. 4(a) and (b)], causing some regions of the cytoplasm to be incorrectly detected as the polar body. Thus, the system pre-processed the image by excluding the cytoplasm from DNN-based detection. The cytoplasm was segmented by image thresholding, and a circular region was determined around its centroid to be excluded from the detection for polar body, as shown in Fig. 4(c).

When an image is input to the trained DNN, a probability map is generated, representing the probability of the polar body's presence in the image. A 5×5 Gaussian filter is used to smooth the probability map, and the position that has maximum intensity exceeding the preset threshold is determined as the position of the polar body [see Fig. 4(c)]. If no position has intensity higher than the preset threshold, the polar body is assumed not to be present in the image, and the system performs out-of-plane orientation control to search for the polar body.

Once the polar body is detected, it is visually tracked by optical flow. Assuming that a 5×5 window around the centroid of the polar body has the same flow vector $\mathbf{d} = [u, v]^T$, the

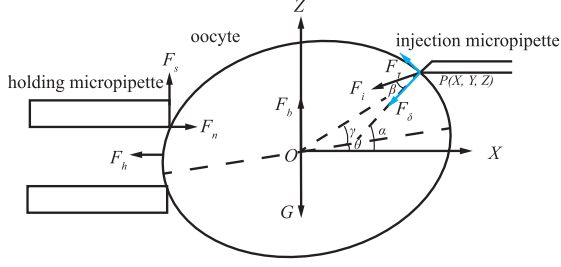


Fig. 5. Force model for deriving the required minimal force to rotate an oocyte. An ellipsoidal oocyte model is used in force analysis to consider oocyte shape differences. Oocyte is gently aspirated by a holding micropipette. An injection micropipette is controlled to indent and rotate the oocyte. The force exerted by the injection micropipette F_i must be sufficient to overcome the friction force F_s between the oocyte and the holding micropipette.

optical flow is

$$\mathbf{R} \cdot \mathbf{d} = \mathbf{T} \quad (2)$$

where \mathbf{R} and \mathbf{T} are the matrices representing spatial and temporal gradients, respectively. The flow vector \mathbf{d} is calculated using the least squares method. The tracked position of the polar body is provided as feedback for in-plane orientation control to rotate the polar body to the target orientation.

IV. MODELING

In oocyte manipulation, the oocyte is aspirated by a holding micropipette with negative pressure, as an unfixed constraint to allow for the relative movement between the oocyte and the holding micropipette. An injection micropipette is controlled to push the oocyte for rotation, and the force applied by the injection micropipette needs to be sufficient to overcome the friction force between the oocyte and the holding micropipette. To achieve minimal oocyte deformation during orientation control, a force model is established to determine the minimal force applied by the injection micropipette to rotate the oocyte.

A. Force Modeling

As shown in Fig. 5, since oocytes are not always spherical and have different ellipticity, an ellipsoidal oocyte model is used in force analysis. For out-of-plane orientation control in the (X, Z) plane, assuming that the oocyte is rotated at a constant speed, force enclosure on the X and Z axes gives

$$F_n - F_h - F_i \cos(\alpha - \beta) = 0 \quad (3)$$

$$F_s + F_b - G - F_i \sin(\alpha - \beta) = 0 \quad (4)$$

where F_n , F_h , and F_s are the support force, aspiration force, and friction force applied by the holding micropipette (unfixed constraint), respectively; F_n is the reaction force to the aspiration force F_h and the force applied by the injection micropipette F_i , and F_i can be divided into a normal component F_δ and a tangent component F_τ ; α is the angle between F_δ and X -axis, and β is the angle between F_i and F_δ ; and F_b and G are the buoyancy and gravity force, respectively.

For an ellipse, $\alpha = \arctan(\frac{a^2}{b^2} \tan \gamma) + \theta$ (see Appendix A). The angle β is determined by the friction coefficient between the

injection micropipette and the oocyte as $\beta = \arctan \mu_I$. Combining (3) and (4), the force exerted by the injection micropipette F_i is

$$F_i = \frac{\mu_H F_h + F_b - G}{\sqrt{1 + \mu_H^2} \sin[\arctan(\frac{a^2}{b^2} \tan \gamma) + \theta - \arctan \mu_I - \arctan \mu_H]} \quad (5)$$

where a and b are the lengths of semimajor and semiminor axes of the ellipse, respectively, γ is the angle between the line connecting indentation position P with the ellipse center O and the ellipse's major axis, θ is the angle between the ellipse's major axis and the X -axis, and μ_I and μ_H are friction coefficients between the injection micropipette and the oocyte and between the holding micropipette and the oocyte, respectively. For in-plane orientation control, force analysis is identical but with buoyancy force F_b and gravity force G in (5) omitted.

During oocyte orientation control, the rotation speed is constant at $30^\circ/\text{s}$. When there is no relative movement between the oocyte and the injection micropipette, angle γ stays unchanged, while angle θ increases with the injection micropipette's movement. Since the initial polar body orientation is random, multiple cycles may be needed to rotate the polar body to the target orientation. In each cycle, the orientation range is $90^\circ - (\theta + \gamma)$, because the injection micropipette is tangent on the oocyte contour and cannot apply tangent force when $\theta + \gamma = 90^\circ$. If the polar body is not rotated to the target orientation within one cycle, the system moves the injection micropipette back to the starting position to initiate the next cycle for orientation control. The starting position is not the same in each cycle. Angle γ determines the starting position of the injection micropipette and satisfies $\arctan(\frac{a^2}{b^2} \tan \gamma) + \theta > \arctan \mu_I + \arctan \mu_H$, since the denominator in (5) must be larger than zero.

According to (5), the force applied by the injection micropipette F_i increases with the increase of aspiration force F_h applied by the holding pipette. A higher aspiration force results in a higher friction force to which the oocyte is subjected when it is rotated relative to the holding micropipette. Thus, it is desired to reduce the aspiration force to reduce F_i and the resulting indentation on the oocyte, but a minimum aspiration force $F_{h_{\min}} = \frac{G - F_b}{\mu_H}$ is required to overcome gravity.

B. Contact Modeling

As illustrated in Fig. 3, after determining the minimal force required for rotating the oocyte, the force value is translated into the indentation depth of the injection micropipette on the oocyte by contact mechanics. Since the deformation around the indentation position is local and small, the Hertzian model [47] is suitable to use for relating the normal force F_δ with indentation depth d

$$F_\delta = F_i \frac{1}{\sqrt{1 + \mu_I^2}} = \frac{2}{\pi} \tan\left(\frac{\lambda}{2}\right) \frac{E}{1 - \nu^2} d^2 \quad (6)$$

where λ is the half-apex angle of the injection micropipette, E is the Young's modulus of the oocyte, and ν is the Poisson's ratio of the oocyte with a typical value of 0.5.

V. ORIENTATION CONTROL

Contact modeling (6) contains the Young's modulus of the oocyte and the friction coefficient between the injection micropipette and the oocyte. Typical values from the literature [39], [40] are used to avoid time-consuming calibration for each oocyte. We are aware that variations in these values among different oocytes could cause the micropipette indentation to be insufficient for inducing a required force to rotate the oocyte, leading to orientation failure. Additionally, the Hertzian model involves approximation (e.g., approximating the micropipette tip as a cone) and could cause inaccuracies in indentation calculation. Thus, an optimal controller is designed to update the indentation for compensating for variations of oocytes' mechanical parameters and potential errors from the contact mechanics model.

A. Optimal Controller Design

The variations of oocytes' mechanical parameters can cause orientation error. Thus, an optimal controller (see Fig. 3) is implemented based on the error between the expected oocyte orientation and the measured orientation from visual feedback. The objective of the optimal controller is to minimize the orientation error and oocyte deformation.

The dynamic equation of oocyte rotation is

$$I\ddot{\theta} + D\dot{\theta} = T_i - T_h \quad (7)$$

where I and D are inertial and damping coefficients; T_i and T_h are torques from injection and holding micropipettes, respectively. Based on (6), we have

$$T_i = \frac{2}{\pi} \tan\left(\frac{\lambda}{2}\right) \frac{\mu_I E l_i}{1 - \nu^2} d^2 = S d^2 \quad (8)$$

where l_i is the distance between the indentation position P and the ellipse center, and S is introduced here to simplify expression. When the force F_i applied by the injection micropipette is sufficient to rotate the oocyte at a constant speed, we have $T_h = T_i = S d^2$. Since variations of μ_I and E among different oocytes can cause F_i to be insufficient for rotating the oocyte, the indentation depth is updated based on the orientation error. The orientation error is incorporated into the system by

$$u = k_p(\theta_d - \theta) + k_d(\dot{\theta}_d - \dot{\theta}) = k_p e + k_d \dot{e} \quad (9)$$

where k_p and k_d are the proportional and derivative gains, θ_d and θ are expected and measured orientation increment of the oocyte in each orientation step, and e is the orientation error. Together, (7)–(9) give

$$k_p e + k_d \dot{e} = S \hat{d}^2 - S d^2 \quad (10)$$

where \hat{d} is the updated indentation, and

$$\hat{d} = \sqrt{d^2 + \frac{1}{S}(k_p e + k_d \dot{e})}. \quad (11)$$

Remark 1: If the orientation error is zero ($e = 0, \dot{e} = 0$), the updated indentation \hat{d} equals the indentation d determined by contact mechanics in (6). The existence of the orientation error

leads to an increased indentation \hat{d} , which the system uses to compensate for the variation of oocytes' mechanical parameters.

To determine the control law for \hat{d} , the state space of the system in (7) is written as

$$\dot{\mathbf{X}} = \mathbf{A}\mathbf{X} + \mathbf{B}u \quad (12)$$

where $\mathbf{X} = [\theta]$, $\mathbf{A} = [0 \ -\frac{1}{I}]$, and $\mathbf{B} = [\frac{1}{I}]$. The constrained optimization problem in (1) is solved by minimizing the cost function

$$J = w_1 \theta^2(t_f) + w_2 \int_{t_0}^{t_f} \hat{d} dt \quad (13)$$

where t_0 is the initial time, t_f is the terminal time, and w_1 and w_2 are weights of orientation error and oocyte deformation, respectively.

Remark 2: In the cost function (13), the quadratic term $\theta^2(t_f)$ represents orientation error, and the integral term $\int_{t_0}^{t_f} \hat{d} dt$ represents oocyte deformation. Their weights are adjusted by tuning w_1 and w_2 .

From (12), locating the minimum of (13) is equivalent to finding the minimum of the following linear quadratic function:

$$J = w_1 \mathbf{X}^T(t_f) \mathbf{X}(t_f) + w_2 \int_{t_0}^{t_f} u^T u dt. \quad (14)$$

Given that the system state \mathbf{X} is measurable, a linear-quadratic regulator controller is designed to minimize the cost function in (14). Its control law is

$$u = -\mathbf{K}\mathbf{X} = -w_2^{-1} \mathbf{B}^T \mathbf{P} \mathbf{X} \quad (15)$$

where $\mathbf{K} = (k_p, k_d)$ is the control gain matrix, and \mathbf{P} is solved from the Riccati equation

$$\mathbf{P}\mathbf{A} + \mathbf{A}^T \mathbf{P} - \mathbf{P}\mathbf{B}w_2^{-1} \mathbf{B}^T \mathbf{P} + \dot{\mathbf{P}} = 0. \quad (16)$$

By substituting \mathbf{K} into (11), the indentation depth to minimize orientation error and oocyte deformation is determined.

Remark 3: The designed optimal controller provides a general form for manipulation with optimization objectives. For the manipulation of deformable objects, other metrics such as object's strain can also be integrated into the cost function. If the cost function cannot be represented in the linear quadratic form and solved from the Riccati equation, the general nonlinear optimal problem can be solved by Hamilton–Jacobi–Bellman equations [48].

B. Path Planning

The indentation position P of the injection micropipette for each orientation increment is determined by the indentation depth d . Path planning is achieved by connecting the indentation positions P of the injection micropipette. For out-of-plane orientation, the indentation position of the injection micropipette is

$$P = \begin{bmatrix} X \\ Z \end{bmatrix} = \begin{bmatrix} \cos\theta & -\sin\theta \\ \sin\theta & \cos\theta \end{bmatrix} \cdot \begin{bmatrix} a \cos\phi \\ b \sin\phi \end{bmatrix} - \begin{bmatrix} \hat{d} \cos\alpha \\ \hat{d} \sin\alpha \end{bmatrix} \quad (17)$$

where $\phi = \arctan(\frac{a}{b}\tan\gamma)$ is the angle in ellipse's parametric equation (see Appendix A). The indentation position of the injection micropipette for in-plane orientation control follows the same path planning but in the (X, Y) plane. Appendix B describes the implementation of the orientation control algorithm.

Remark 4: Orientation control in this article is designed for an ellipsoidal object (i.e., an oocyte), but the modeling, control, and path planning approaches can be readily expanded to the orientation control of a deformable object having an arbitrary shape.

VI. EXPERIMENTAL RESULTS AND DISCUSSION

A. Polar Body Detection Results

To collect data for DNN training, 1000 oocyte images with polar bodies of different sizes, shapes, and focus were captured. The positions of polar bodies were labeled manually. The pixel at the center of the polar body was labeled as 1, while other pixels were labeled as 0. For each image, image patches (square windows of 50×50 pixels) were obtained across the image, and each image patch was labeled as the same class as its central pixel. After data balancing as discussed in Section III, a total of 278 563 image patches were collected, with a balanced distribution of classes (149 700 in Class 1 and 128 863 in Class 0). The dataset was separated into 80% for training, 10% for validation, and 10% for test. The trained networks provided an accuracy of 99.5% for polar body detection in the test set.

To further evaluate the performance of the trained DNN, 300 additional oocyte images were captured for testing. Image preprocessing was performed to remove the interference from the cytoplasm, as discussed in Section III. In DNN training, the training set comprised polar body images captured when polar bodies were out of focus, so the trained DNN can detect an out-of-focus polar body in an image. DNN-based polar body detection also has robustness to variations of polar bodies' sizes and shapes. In comparison, image thresholding and edge detection [13], [43] are not capable of detecting polar bodies that are out of focus.

The polar body was regarded to be successfully detected if the detected position by the DNN was closer than 10 pixels ($3.6 \mu\text{m}$ under $20\times$ microscope objective) to the manually labeled position of the polar body. We used receiver operating characteristics (ROC) and precision recall (PR) curves to evaluate the performance of the DNN models. When the classification threshold is varied, the ROC curve plots sensitivity versus false positive rate (i.e., $1 - \text{specificity}$), and the PR curve plots precision versus sensitivity. Sensitivity measures, among image patches with polar bodies, how many are correctly identified. False positive rate measures, among image patches without polar bodies, how many are falsely identified as polar bodies. Specificity measures, among image patches without polar bodies, how many are correctly identified as without polar bodies. Precision measures, among image patches identified as polar bodies, how many are correctly identified. Fig. 6(a) shows ROC curves of the trained DNN models on polar body detection. The performance of the classifier was evaluated by the area under curve (AUC). A random classifier (the dashed line) only has an AUC of 0.50.

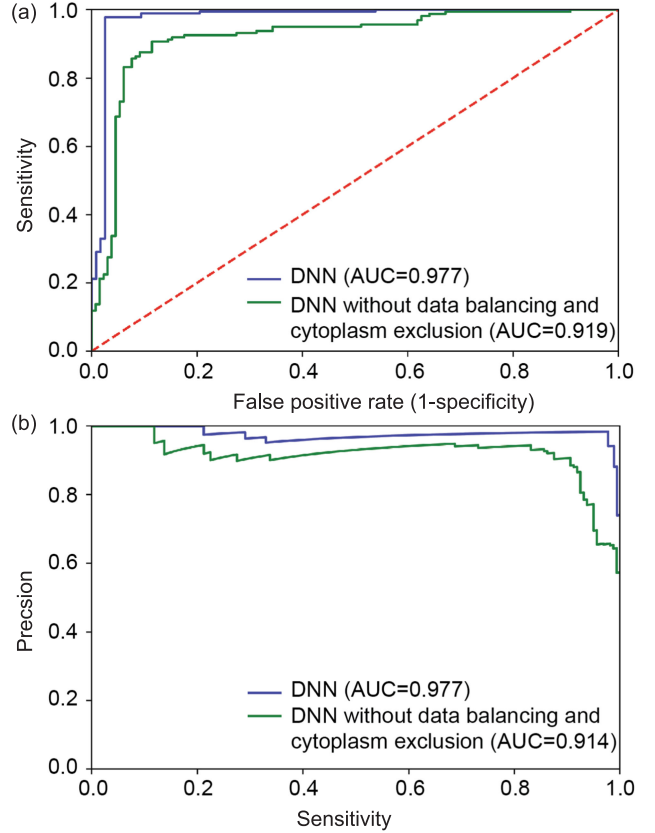


Fig. 6. (a) ROC curves of the trained DNN models for polar body detection. The trained DNN achieved an AUC of 0.977. The DNN without data balancing and cytoplasm exclusion achieved a lower AUC of 0.919. (b) PR curve of the trained DNN models for polar body detection. The trained DNN achieved an AUC of 0.977. In comparison, the DNN without data balancing and cytoplasm exclusion only achieved an AUC of 0.914.

The trained DNN achieved an AUC of 0.977 ($n = 300$; 95% CI, 0.955–0.991), while the DNN without data balancing and cytoplasm exclusion only achieved an AUC of 0.919 ($n = 300$; 95% CI, 0.884–0.955). PR curves of the trained DNN models are shown in Fig. 6(b). The trained DNN achieved an AUC of 0.977 ($n = 300$; 95% CI, 0.955–0.990). In comparison, the DNN without data balancing and cytoplasm exclusion only achieved an AUC of 0.914 ($n = 300$; 95% CI, 0.881–0.946).

When setting the threshold to be 0.33, the trained DNN achieved 97.6% in accuracy, 98.3% in precision, 97.8% in sensitivity, 97.4% in specificity, and 98.0% in F_1 score (see Table I for definition of the metrics). In addition, accuracy measures, among all image patches, how many are correctly identified, and F_1 is the harmonic mean of precision and sensitivity. Error occurred when only a small part (less than 5%) of a polar body was present in an image. The maximum value in the probability map did not exceed the preset threshold; thus, it was not detected as a polar body. When the threshold was set to be lower, more false positive cases arose due to interferences from microparticles sometimes present in culture medium. So, the threshold was tuned in DNN training to effectively distinguish polar bodies while overcoming the interferences. It should be noted that when the DNN did not detect the presence of a polar body, it did not cause robotic

TABLE I
PERFORMANCE OF DNN FOR POLAR BODY DETECTION

Metric	Definition	Performance(%)	
		DNN	DNN without data balancing and cytoplasm exclusion
Accuracy	$\frac{TP+TN}{Sum}$	97.6	90.5
Precision	$\frac{TP}{TP+FP}$	98.3	93.6
Sensitivity	$\frac{TP}{TP+FN}$	97.8	90.4
Specificity	$\frac{TN}{FP+TN}$	97.4	90.5
F ₁ score	$\frac{2TP}{2TP+FP+FN}$	98.0	92.0

TP: true positive, TN: true negative, FP: false positive, FN: false negative.

orientation control to fail because in such a case, the system continued with out-of-plane orientation control to search for the polar body until rotating the polar body into the focal plane. The required time for detection of polar body is 0.2 s (Intel i7 processor, Nvidia GTX1080 GPU).

We also evaluated the performance of the DNN for polar body detection using the same threshold but without data balancing and cytoplasm exclusion. When data balancing and cytoplasm exclusion were not conducted, the polar body detection accuracy dropped to 90.5%, and precision, sensitivity, specificity, and F₁ score also became significantly lower, as summarized in Table I. These results proved the importance of data balancing and cytoplasm exclusion for the DNN to achieve satisfactory performance in polar body detection.

B. Orientation Control Results

The system achieved robotic orientation control of oocytes by controlling the injection micropipette to push/indent the oocyte. Robotic orientation control of an ellipsoidal oocyte is shown in Fig. 7 (also see the supplementary video). When the polar body was not present in the microscope focal plane, out-of-plane orientation control was performed to search for the polar body. Once the polar body was detected by DNNs, it was rotated to the focal plane. As shown in Fig. 7(b), the polar body was at around 5 o'clock orientation, and the robotic system continued with in-plane orientation control to rotate the polar body toward the target orientation of 12 o'clock. Limited by the range of rotation in one cycle, after the first cycle of orientation control [see Fig. 7(c) and (d)], the polar body was rotated to around 2 o'clock orientation. So, the injection micropipette moved back to its starting position to initiate the second cycle of orientation control to rotate the polar body to the target orientation [see Fig. 7(e) and (f)].

The manipulation path of the injection micropipette was designed in this article to rotate the oocyte with minimal oocyte deformation. As detailed in Section V, for designing the manipulation path, the required minimal force to rotate the oocyte was determined by the force model (5) and was then translated into micropipette indentation on the oocyte using contact mechanics (6). The manipulation path was formed by connecting the indentation positions according to (17). Because contact mechanics involves the mechanical parameters of the oocyte

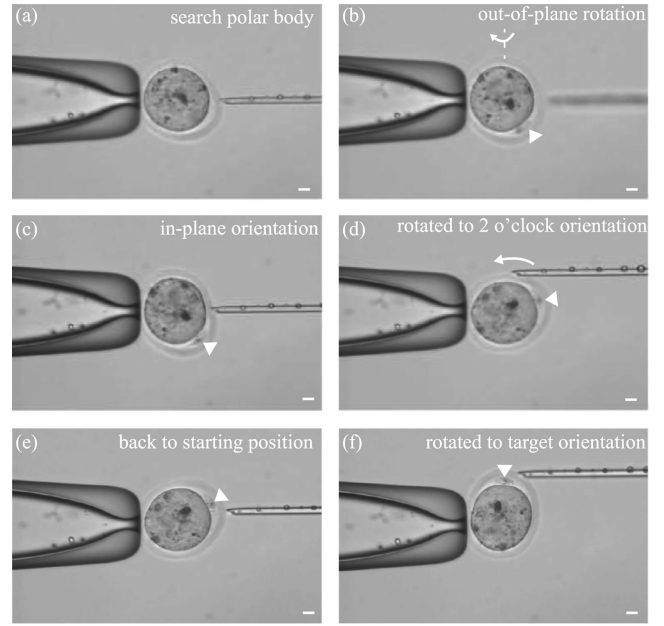


Fig. 7. Robotic orientation of an ellipsoidal oocyte. Polar body is labeled with a triangle. Scale bar: 10 μm . (a) Polar body was not present in the focal plane. (b) System performed out-of-plane orientation control, searched for the polar body, and rotated it into the focal plane. (c) and (d) In-plane orientation control was followed by the system to rotate the polar body toward the target orientation of 12 o'clock. (e) and (f) Second cycle of in-plane orientation control.

(Young's modulus and friction coefficient), typical values from the literature were used to avoid time-consuming calibration. To reduce the orientation errors caused by the oocyte variations, an optimal controller (11) was designed based on the orientation error. The optimal controller updated the indentation to ensure the application of a sufficient force with minimal deformation maintained.

To quantitatively evaluate the performance of the proposed orientation control method, experiments were performed on 15 mouse oocytes, and for each oocyte, orientation control was repeated ten times. Before each experiment, the oocyte was repelled from the holding micropipette by applying a positive pressure and then aspirated back to randomize its initial orientation. Orientation control was performed to rotate the polar body to the target orientation of 12 o'clock. Oocyte deformation and orientation error were both quantified during each orientation control process. Oocyte deformation was measured as the indentation of the detected contour of the zona pellucida. For out-of-plane orientation control, the indentation was difficult to observe; thus, it was calculated as the distance between the injection micropipette tip and the oocyte contour. The out-of-plane oocyte contour was obtained by rotating the in-plane contour around its major axis. The position of the micropipette tip was determined from the known movement of the micromanipulator motors.

Fig. 8(a) shows the manipulation path of the injection micropipette to rotate an oocyte with an ellipticity of 0.16 for 70°. Ellipticity was defined as

$$\text{ellipticity} = \frac{a-b}{a} \quad (18)$$

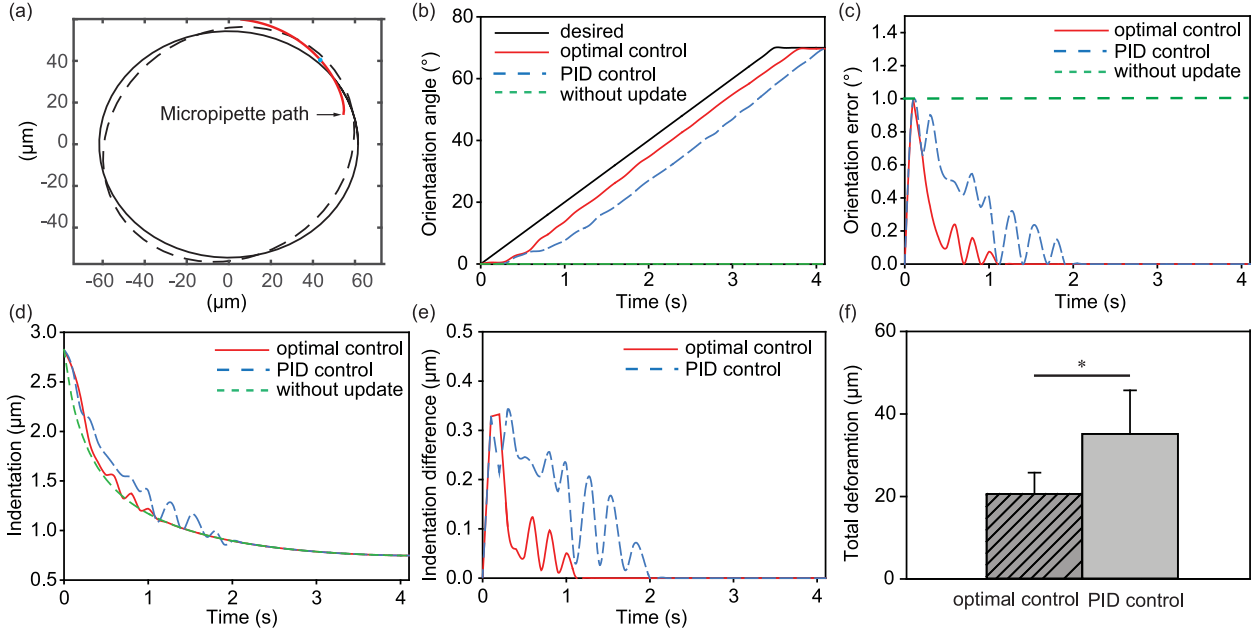


Fig. 8. (a) Manipulation path of the injection micropipette for rotating an oocyte with an ellipticity of 0.16 for 70° . Solid ellipse represents the oocyte at the starting orientation. Dashed ellipse represents the oocyte at 30° orientation, and the enlarged dot on the motion path was the micropipette indentation position when the oocyte reached the 30° orientation. (b) When indentation was determined only by contact mechanics (without indentation update), the force applied by the injection micropipette was insufficient to rotate the oocyte and the orientation angle was kept at 0° . The optimal controller and PID controller both updated the indentation depth based on the feedback of orientation errors, and both reached the target orientation of 70° . (c) During the orientation process, orientation control without indentation update had a constant orientation error of 1° . The optimal controller reduced the orientation error to zero faster than the PID controller. (d) Injection micropipette's indentation on the oocyte during orientation control. The optimal controller in general introduced less oocyte deformation compared to the PID controller. Indentation without update was insufficient to rotate the oocyte; thus, the optimal controller and the PID controller both updated (increased) the indentation depth based on the orientation errors. (e) Differences of updated indentation by the optimal and PID controllers than indentation by contact mechanics. (f) Total/Cumulative oocyte deformation before the orientation error was reduced to zero. The total deformation of the optimal control was significantly less than that of PID control ($P < 0.01$). For each controller, $n = 50$ tests, ten repeated experiments per oocyte, five oocytes.

where a and b are the lengths of semimajor and semiminor axes of an ellipse/oocyte, respectively. The solid ellipse was the oocyte at the starting orientation. The dashed ellipse shows the oocyte at 30° orientation, and the enlarged dot denotes the indentation position of the injection micropipette when the oocyte reached the 30° orientation. The enlarged dot is inside (versus on) the oocyte contour (dashed ellipse) because of the slight indentation of the micropipette on the oocyte.

Fig. 8(b) illustrates an orientation process using different control strategies. The desired curve corresponds to the case when the oocyte is rotated at a constant speed (1° per step) without any slippage of the injection micropipette. In experiments, when indentation was only calculated/set by contact mechanics (without indentation update) for this oocyte, the injection micropipette slipped on the oocyte and the orientation angle was kept at 0° . This is because if the oocyte's actual friction coefficient with the injection micropipette μ_i or actual Young's modulus E is lower than the preset values [see (6)], the force induced by the indentation d becomes lower than the required minimal force F_i in (5) and insufficient to rotate the oocyte. To prevent orientation failure, the orientation error was used as feedback for indentation compensation/update. Orientation control was implemented using the designed optimal controller and for comparison, also using PID control, and the performance was quantitatively compared. Optimal control gains in (11) were calculated set to be $k_p = 0.077$ and $k_d = 0.0091$. The PID

controller updated the indentation depth \hat{d} according to

$$\hat{d} = d + k_P e + k_I \int e + k_D \dot{e} \quad (19)$$

where d is the indentation depth determined by contact mechanics. k_P , k_I , and k_D are proportional, integral, and derivative gains, respectively. The PID gains were tuned through extensive experiments and set to be $k_P = 0.40$, $k_I = 0.05$, and $k_D = 0.08$.

As shown in Fig. 8(b), although under the optimal control and the PID control, the micropipette at first slipped on the oocyte (deviated from the desired curve), the updated indentation based on the orientation error ensured sufficient force to be applied for oocyte rotation and overcame the slip (paralleled with the desired curve). Both control strategies reached the target orientation of 70° with an error less than 0.3° . In this orientation process, the optimal controller overcame the slip faster than the PID controller. We then analyzed the orientation errors. In (9), the orientation error was defined as the difference between the expected and measured orientation increments in an orientation step. Fig. 8(c) shows orientation errors in this orientation process. It can be seen that orientation control without indentation update had a constant orientation error of 1° in each orientation step; the optimal controller reduced the orientation error to 0 faster than the PID controller (1.2 s versus 1.8 s). Also importantly, the optimal controller introduced less indentation

(i.e., oocyte deformation) compared to the PID controller [see Fig. 8(d)]. When comparing the total deformation before the orientation error was reduced to 0, the optimal control achieved a total deformation of $20.72 \mu\text{m}$ (versus $30.58 \mu\text{m}$ for PID control). Note that in Fig. 8(d), the indentation depth determined by contact mechanics was less than that of the optimal controller and the PID controller, but it was insufficient to rotate the oocyte. The maximum deformation for this oocyte was $2.82 \mu\text{m}$. Oocyte deformation decreased with the increase of orientation angle because the force F_i required to rotate the oocyte decreased when the orientation angle θ increased [see (5)].

To illustrate the indentation difference more clearly, Fig. 8(e) plots the differences of updated indentation by optimal control and PID control than the indentation by contact mechanics, i.e., $\Delta d = \hat{d} - d$. It can be seen that the optimal controller generally resulted in less indentation in the orientation process. To further validate the superiority of the optimal controller over the PID controller, we compared the cumulative oocyte deformation before the orientation error reached zero using each control strategy on five oocytes (ten repeated experiments per oocyte). As shown in Fig. 8(f), the optimal controller achieved a total deformation of $20.61 \pm 5.16 \mu\text{m}$, significantly less than the total oocyte deformation of $35.19 \pm 10.53 \mu\text{m}$ by the PID controller ($n = 50$ for each control strategy, $P < 0.01$ using the t -test). The optimal controller incorporated both the orientation error and oocyte deformation into the cost function (13); therefore, oocyte deformation was minimized while reducing the orientation error.

Fig. 9(a) shows the maximum deformation for each of the tested 15 oocytes during orientation control ($n = 10$ tests for each oocyte). Our orientation control strategy achieved $2.70 \pm 0.37 \mu\text{m}$ in maximum deformation, and oocyte deformation was consistently below $4 \mu\text{m}$ for each oocyte. As summarized in Fig. 9(a), these oocytes had different ellipticity defined in (18), ranging from 0.007 to 0.203, and the smaller the ellipticity is, the closer the oocyte contour resembles a circle (a standard circle has ellipticity of 0). Among the oocytes, 11 out of 15 had ellipticity over 0.1, confirming the need for the development of the orientation control strategy based on an ellipsoid oocyte model.

For understanding purposes, we randomly chose five oocytes and quantitatively measured their Young's modulus by micropipette aspiration, in which the aspiration pressure was increased from 200 Pa to 2 kPa with a step of 200 Pa, and each step lasted 30 s. The aspirated lengths of the zona pellucida inside the micropipette were recorded to determine the Young's modulus based on the shell model [40]. Fig. 9(b) shows that the oocytes had Young's modulus values ranging from 10.2 to 17.3 kPa, and their maximum deformation was consistently kept under $4 \mu\text{m}$ during robotic orientation control. The results showed that our robotic orientation control strategy achieved small oocyte deformations and was robust to oocyte heterogeneity in shapes and mechanical parameters.

The mouse oocytes had a radius around $60 \mu\text{m}$ and zona pellucida thickness around $8 \mu\text{m}$. The deformation of $2.70 \mu\text{m}$ only accounts for 4% of the oocyte radius and one-third of the zona pellucida's thickness. In comparison, previous oocyte orientation control using micropipettes [39] resulted in an average

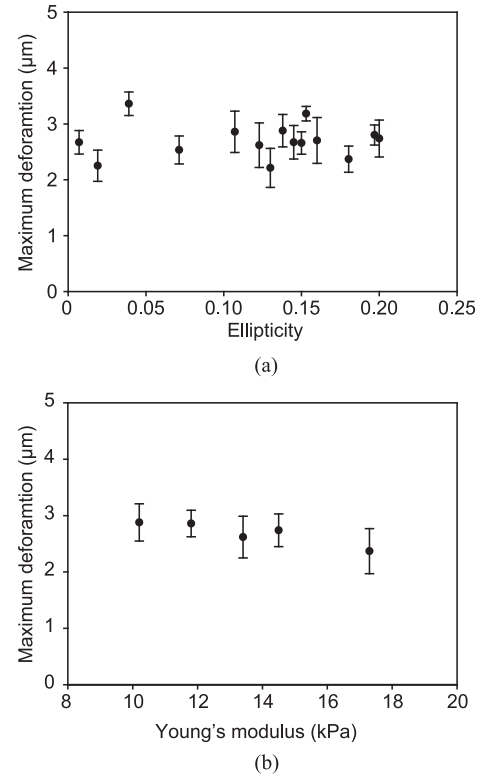


Fig. 9. (a) Maximum deformation of 15 oocyte in orientation control. $n = 10$ for each oocyte. The oocytes have different ellipticity ranging from 0.007 to 0.203, and the maximum deformation was $2.70 \pm 0.37 \mu\text{m}$. (b) For understanding purposes, five oocytes were randomly chosen to measure their Young's modulus, and their maximum deformation during orientation control were consistently under $4 \mu\text{m}$. Robotic orientation control achieved very small oocyte deformation and was robust to oocyte heterogeneity in shapes and mechanical parameters.

oocyte deformation of $11.7 \mu\text{m}$ because the mammalian oocyte was modeled as a sphere rather than an ellipsoid, which is more common among mammalian oocytes. The improper assumption of the spherical shape led to large indentation of the injection micropipette on the oocyte and thus the undesired large deformations. Compared to mammalian oocytes, the orientation control of zebrafish embryos [19] is a significantly less challenging task because zebrafish embryos are large ($\sim 1 \text{ mm}$ in diameter) and are much less deformable (Young's modulus of zebrafish embryos: $\sim 1.5 \text{ MPa}$ versus mouse oocytes: $< 20 \text{ kPa}$).

To quantify the accuracy of orientation control, orientation error was defined as the difference between the final orientation of the polar body and the target orientation. For the experiments performed by the robotic system, orientation error was determined to be $0.7 \pm 0.3^\circ$ ($n = 150$). The nonzero orientation error was mainly due to microscopy imaging resolution, which limited the selection of the orientation control increment [$\Delta\theta$ in (1)] to 1° .

Robotic oocyte orientation control was compared with manual rotation performed by experienced embryologists at the Toronto CRATe Fertility Centre. The time cost for orienting an oocyte was comparable between manual rotation and robotic control (10–15 s); however, the robotic system, due to modeling, optimal control, and path planning, achieved significantly less oocyte

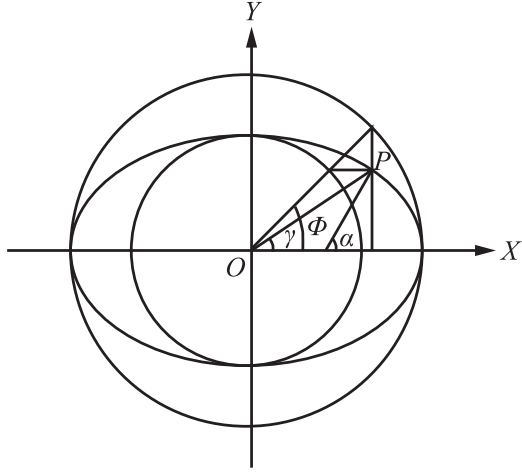


Fig. 10. Geometric analysis of an ellipse.

deformation ($2.70 \mu\text{m}$ versus $>10 \mu\text{m}$) and orientation errors (0.7° versus $> 2^\circ$).

VII. CONCLUSION

This article presented robotic orientation control of deformable cells for both out-of-plane and in-plane rotation. Orientation control was achieved using a clinical setup of two glass micropipettes. For detecting the polar body of an oocyte, DNNs were developed with robustness to variations of polar bodies' shapes and sizes (accuracy: 97.6%). The manipulation path of the micropipette was planned to rotate the oocyte with minimal oocyte deformation. Modeling was performed to determine the required minimal force to rotate an ellipsoidal oocyte and the corresponding micropipette indentation on the oocyte. An optimal controller was developed to update the indentation based on the visual feedback of orientation errors and was proven to be effective for compensating for the variations of oocytes' mechanical parameters. The robotic system achieved orientation control with an accuracy of 0.7° and the maximum oocyte deformation of $2.70 \mu\text{m}$.

APPENDIX A GEOMETRIC ANALYSIS

As shown in Fig. 10, assuming that a point $P_0(x_0, y_0)$ is on the ellipse, α is the angle between its normal line on the ellipse and the X -axis, and γ is the angle between its connecting line with the ellipse center O and the ellipse's major axis. ϕ is the corresponding angle of P_0 in ellipse' parametric equation, and P_0 can be expressed as $(a\cos\phi, b\sin\phi)$, with a and b the lengths of semimajor and semiminor axes of the ellipse. We have

$$\tan\gamma = \frac{b\sin\phi}{a\cos\phi} = \frac{b}{a}\tan\phi. \quad (20)$$

Denote the angle between the ellipse's major axis and the X -axis as θ . When $\theta = 0$, the slope of the normal line on P_0 is

$$\tan\alpha = \frac{y_0 a^2}{x_0 b^2} = \frac{a}{b}\tan\phi = \frac{a^2}{b^2}\tan\gamma. \quad (21)$$

When the ellipse is rotated with an angle of $\theta > 0$, $\alpha = \arctan\left(\frac{a^2}{b^2}\tan\gamma\right) + \theta$.

APPENDIX B

IMPLEMENTATION OF THE ORIENTATION CONTROL ALGORITHM

-
- 1: Formulate linear quadratic cost function in (14)
 - 2: Solve Riccati equation for control gain $\mathbf{K} \leftarrow (16)$
 - 3: **While** orientation error $|e| \geq \epsilon$ **do**
 - 4: Determine the minimal force $F_i \leftarrow (5)$
 - 5: Compute micropipette indentation $d \leftarrow (6)$
 - 6: Measure error e from visual feedback
 - 7: Update micropipette indentation $\hat{d} \leftarrow (11)$
 - 8: Compute micropipette position $P \leftarrow (17)$
 - 9: Command robot motion
 - 10: **End while**
-

REFERENCES

- [1] M. Saadat and P. Nan, "Industrial applications of automatic manipulation of flexible materials," *Ind. Robot*, vol. 29, no. 5, pp. 434–442, 2002.
- [2] S. Miller, J. van den Berg, M. Fritz, T. Darrell, K. Goldberg, and P. Abbeel, "A geometric approach to robotic laundry folding," *Int. J. Robot. Res.*, vol. 31, no. 2, pp. 249–267, 2012.
- [3] A. Shademan, R. S. Decker, J. D. Opfermann, S. Léonard, A. Krieger, and P. C. W. Kim, "Supervised autonomous robotic soft tissue surgery," *Sci. Transl. Med.*, vol. 8, no. 337, 2016, Art. no. 337ra64.
- [4] J. Sanchez, J.-A. Corrales, B.-C. Bouzgarrou, and Y. Mezouar, "Robotic manipulation and sensing of deformable objects in domestic and industrial applications: A survey," *Int. J. Robot. Res.*, vol. 37, no. 7, pp. 688–716, 2018.
- [5] S. Hu and D. Sun, "Automatic transportation of biological cells with a robot-tweezer manipulation system," *Int. J. Robot. Res.*, vol. 30, no. 14, pp. 1681–1694, 2011.
- [6] X. Liu, K. Kim, Y. Zhang, and Y. Sun, "Nanonewton force sensing and control in microrobotic cell manipulation," *Int. J. Robot. Res.*, vol. 28, no. 8, pp. 1065–1076, 2009.
- [7] S. Permana, E. Grant, G. M. Walker, and J. A. Yoder, "A review of automated microinjection systems for single cells in the embryogenesis stage," *IEEE/ASME Trans. Mechatronics*, vol. 21, no. 5, pp. 2391–2404, Oct. 2016.
- [8] P. Devroey and A. Van Steirteghem, "A review of ten years experience of ICSI," *Human Reproduction Update*, vol. 10, no. 1, pp. 19–28, 2004.
- [9] M. Montag, K. van der Ven, B. Rösing, and H. H. B. van der Ven, "Polar body biopsy: A viable alternative to preimplantation genetic diagnosis," *Reproductive Biomed. Online*, vol. 1, pp. 6–11, 2009.
- [10] A. Greenfield, P. Braude, F. Flinter, R. L.-Badge, C. Ogilvie, and A. C. F. Perry, "Assisted reproductive technologies to prevent human mitochondrial disease transmission," *Nature Biotechnol.*, vol. 35, pp. 1059–1068, 2017.
- [11] H. Yang, H. Wang, C. S. Shivalila, A. W. Cheng, L. Shi, and R. Jaenisch, "One-step generation of mice carrying reporter and conditional alleles by CRISPR/Cas-mediated genome engineering," *Cell*, vol. 154, no. 6, pp. 1370–1379, 2013.
- [12] P. Rubino, P. Viganó, A. Luddi, and P. Piomboni, "The ICSI procedure from past to future: A systematic review of the more controversial aspects," *Human Reproduction Update*, vol. 22, no. 2, pp. 194–227, 2016.
- [13] C. Leung, Z. Lu, X. P. Zhang, and Y. Sun, "Three-dimensional rotation of mouse embryos," *IEEE Trans. Biomed. Eng.*, vol. 59, no. 4, pp. 1049–1056, Apr. 2012.
- [14] M. Hagiwara, K. Tomohiro, and A. Fumihito, "Local streamline generation by mechanical oscillation in a microfluidic chip for noncontact cell manipulations," *Appl. Phys. Lett.*, vol. 101, no. 7, 2012, Art. no. 074102.
- [15] M. Xie, J. K. Mills, Y. Wang, M. Mahmoodi, and D. Sun, "Automated translational and rotational control of biological cells with a robot-aided optical tweezers manipulation system," *IEEE Trans. Autom. Sci. Eng.*, vol. 13, pp. 543–551, Apr. 2016.

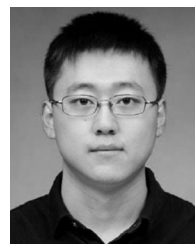
- [16] H. Zhang and K.-K. Liu, "Optical tweezers for single cells," *J. Roy. Soc. Interface*, vol. 5, no. 24, pp. 671–690, 2008.
- [17] H. Shafiee, J. L. Caldwell, M. B. Sano, and R. V. Davalos, "Contactless dielectrophoresis: A new technique for cell manipulation," *Biomed. Microdevices*, vol. 11, no. 5, pp. 997–1006, 2009.
- [18] X. Liu, Z. Lu, and Y. Sun, "Orientation control of biological cells under inverted microscopy," *IEEE/ASME Trans. Mechatronics*, vol. 16, no. 5, pp. 918–924, Oct. 2011.
- [19] Z. Wang, C. Feng, R. Muruganandam, W. T. Ang, S. Y. M. Tan, and W. T. Latt, "Three-dimensional cell rotation with fluidic flow-controlled cell manipulating device," *IEEE/ASME Trans. Mechatronics*, vol. 21, no. 4, pp. 1995–2003, Aug. 2016.
- [20] M. Hagiwara, T. Kawahara, Y. Yamanishi, and T. Masuda, "On-chip magnetically actuated robot with ultrasonic vibration for single cell manipulations," *Lab on a Chip*, vol. 11, pp. 2049–2054, 2011.
- [21] A. M. Bilek, K. C. Dee, and D. P. Gaver, III, "Mechanisms of surface-tension-induced epithelial cell damage in a model of pulmonary airway reopening," *J. Appl. Physiol.*, vol. 94, no. 2, pp. 770–783, 2003.
- [22] Z. Luo *et al.*, "Deformation of a single mouse oocyte in a constricted microfluidic channel," *Microfluidics Nanofluidics*, vol. 19, no. 4, pp. 883–890, 2015.
- [23] K. Yanagida, H. Katayose, H. Yazawa, Y. Kimura, K. Konnai, and A. Sato, "The usefulness of a piezo-micromanipulator in intracytoplasmic sperm injection in humans," *Human Reproduction*, vol. 14, no. 2, pp. 448–453, 1999.
- [24] Z. Nagy *et al.*, "The influence of the site of sperm deposition and mode of oolemma breakage at intracytoplasmic sperm injection on fertilization and embryo development rates," *Human Reproduction*, vol. 10, no. 12, pp. 3171–3177, 1995.
- [25] M. Higashimori, K. Yoshimoto, and M. Kaneko, "Active shaping of an unknown rheological object based on deformation decomposition into elasticity and plasticity," in *Proc. IEEE Int. Conf. Robot. Autom.*, 2010, pp. 5120–5126.
- [26] H. Lin, F. Guo, F. Wang, and Y.-B. Jia, "Picking up a soft 3D object by feeling the grip," *Int. J. Robot. Res.*, vol. 34, no. 11, pp. 1361–1384, 2015.
- [27] J. Smolen and A. Patriciu, "Deformation planning for robotic soft tissue manipulation," in *Proc. 2nd Int. Conf. Adv. Comput.-Human Interact.*, 2009, pp. 199–204.
- [28] D. Navarro-Alarcón, Y.-H. Liu, J. G. Romero, and P. Li, "Model-free visually servoed deformation control of elastic objects by robot manipulators," *IEEE Trans. Robot.*, vol. 29, no. 6, pp. 1457–1468, Dec. 2013.
- [29] D. Navarro-Alarcon *et al.*, "Automatic 3-D manipulation of soft objects by robotic arms with an adaptive deformation model," *IEEE Trans. Robot.*, vol. 32, no. 2, pp. 429–441, Apr. 2016.
- [30] F. Lamiroux and L. E. Kavraki, "Planning paths for elastic objects under manipulation constraints," *Int. J. Robot. Res.*, vol. 20, pp. 188–208, 2001.
- [31] M. Moll and L. E. Kavraki, "Path planning for deformable linear objects," *IEEE Trans. Robot.*, vol. 22, no. 4, pp. 625–636, Aug. 2006.
- [32] G. Duchemin, P. Maillet, P. Poignet, E. Dombre, and F. Pierrot, "A hybrid position/force control approach for identification of deformation models of skin and underlying tissues," *IEEE Trans. Biomed. Eng.*, vol. 52, no. 2, pp. 160–170, Feb. 2005.
- [33] Y. Xie, D. Sun, C. Liu, H. Y. Tse, and S. H. Cheng, "A force control approach to a robot-assisted cell microinjection system," *Int. J. Robot. Res.*, vol. 29, pp. 1222–1232, 2010.
- [34] L. De Santis *et al.*, "Polar body morphology and spindle imaging as predictors of oocyte quality," *Reproductive Biomed. Online*, vol. 11, no. 1, pp. 36–42, 2005.
- [35] B. Balaban and B. Urman, "Effect of oocyte morphology on embryo development and implantation," *Reproductive Biomed. Online*, vol. 12, no. 5, pp. 608–615, 2006.
- [36] M. Saha and P. Isto, "Manipulation planning for deformable linear objects," *IEEE Trans. Robot.*, vol. 23, no. 6, pp. 1141–1150, Dec. 2007.
- [37] Z. Zhang, X. Wang, J. Liu, C. Dai, and Y. Sun, "Robotic micromanipulation: Fundamentals and applications," *Annu. Rev. Control, Robot., Auton. Syst.*, vol. 2, pp. 181–203, 2019.
- [38] C. Dai *et al.*, "Robotic orientation control of deformable cells," in *Proc. IEEE Int. Conf. Robot. Autom.*, 2019, pp. 8980–8985.
- [39] Q. Zhao, M. Sun, M. Cui, J. Yu, Y. Qin, and X. Zhao, "Robotic cell rotation based on the minimum rotation force," *IEEE Trans. Autom. Sci. Eng.*, vol. 12, pp. 1504–1515, Oct. 2015.
- [40] M. Khalilian, M. Navidbakhsh, M. R. Valojerdi, M. Chizari, and P. E. Yazdi, "Estimating Young's modulus of zona pellucida by micropipette aspiration in combination with theoretical models of ovum," *J. Roy. Soc. Interface*, vol. 7, no. 45, pp. 687–694, 2010.
- [41] W.-H. Wang, L. Meng, R. J. Hackett, R. Odenbourg, and D. L. Keefe, "Limited recovery of meiotic spindles in living human oocytes after cooling—Rewarming observed using polarized light microscopy," *Human Reproduction*, vol. 16, no. 11, pp. 2374–2378, 2001.
- [42] J. E. Swain, "Optimizing the culture environment in the IVF laboratory: Impact of pH and buffer capacity on gamete and embryo quality," *Reproductive Biomed. Online*, vol. 21, no. 1, pp. 6–16, 2010.
- [43] Z. Wang, C. Feng, W. T. Ang, S. Y. M. Tan, and W. T. Latt, "Autofocusing and polar body detection in automated cell manipulation," *IEEE Trans. Biomed. Eng.*, vol. 64, no. 5, pp. 1099–1105, May 2017.
- [44] G. Litjens *et al.*, "A survey on deep learning in medical image analysis," *Med. Image Anal.*, vol. 42, pp. 60–88, 2017.
- [45] T. Falk *et al.*, "U-net: Deep learning for cell counting, detection, and morphometry," *Nature Methods*, vol. 16, no. 1, pp. 67–70, 2019.
- [46] F. Xing, Y. Xie, and L. Yang, "An automatic learning-based framework for robust nucleus segmentation," *IEEE Trans. Med. Imag.*, vol. 35, no. 2, pp. 550–566, Feb. 2016.
- [47] C. T. McKee, J. A. Last, P. Russell, and C. J. Murphy, "Indentation versus tensile measurements of Young's modulus for soft biological tissues," *Tissue Eng. Part B: Rev.*, vol. 17, no. 3, pp. 155–164, 2011.
- [48] F. Lin, *Robust Control Design: An Optimal Control Approach*, vol. 18. Hoboken, NJ, USA: Wiley, 2007.



Changsheng Dai received the B.E. and M.E. degrees in mechanical engineering from the Harbin Institute of Technology, Harbin, China, in 2014 and 2016, respectively. He is currently working toward the Ph.D. degree in mechanical engineering with the University of Toronto, Toronto, ON, Canada.

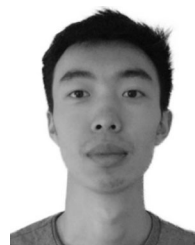
His research interests include robotic cell manipulation and medical robotics.

Mr. Dai was a recipient of the Best Paper Award in Automation at the IEEE International Conference on Robotics and Automation in 2019.



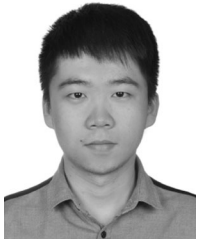
Zhuoran Zhang received the B.E. degree in automation from the Harbin Institute of Technology, Harbin, China, in 2014, and the Ph.D. degree in mechanical engineering from the University of Toronto, Toronto, ON, Canada, in 2019.

He is currently a Postdoctoral Fellow with the Advanced Micro and Nanosystems Laboratory, University of Toronto. His research interests include robotic cell manipulation, automation at micro/nano scales, and medical robotics.



Yuchen Lu received the B.A.Sc. degree in mechanical engineering from the University of Toronto, Toronto, ON, Canada, in 2019. He is currently working toward the M.S. degree in electrical and computer engineering with the University of California, San Diego, CA, USA.

His research interests include simultaneous localization and mapping, computer vision, and sensor fusion.



Guanqiao Shan received the B.E. degree in electronic information and the M.S. degree in physics from Beihang University, Beijing, China, in 2014 and 2017, respectively. He is currently working toward the Ph.D. degree in mechanical engineering with the University of Toronto, Toronto, ON, Canada.

His research interests include robotic cell manipulation and characterization.



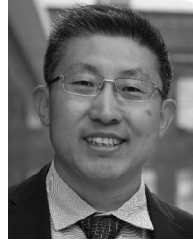
Changhai Ru received the Ph.D. degree in mechanical engineering from the Harbin Institute of Technology, Harbin, China, in 2005.

He became an Associate Professor in 2005 and a Full Professor in 2007 with Soochow University, Suzhou, China. His research specializes in developing micro/nano technologies and instruments for manipulating and drug spraying.



Xian Wang received the bachelor's degree in engineering from Tianjin University, Tianjin, China, in 2015. He is currently working toward the Ph.D. degree in mechanical engineering with the Department of Mechanical and Industrial Engineering and the Institute of Biomaterials and Biomedical Engineering, University of Toronto, Toronto, ON, Canada.

His current research interests include magnetic microrobots for biomedical applications.



Yu Sun (F'14) received the Ph.D. degree in mechanical engineering from the University of Minnesota, Minneapolis, MN, in 2003. He is a Professor with the University of Toronto, Toronto, ON, Canada, where he is a Tier I Canada Research Chair and Director of the Robotics Institute. His laboratory specializes in developing innovative technologies and instruments for manipulating and characterizing cells, molecules, and nanomaterials.

Prof. Sun is a Fellow of the American Society of Mechanical Engineers, the American Association for the Advancement of Science, the National Academy of Inventors, the Canadian Academy of Engineering, and the Royal Society of Canada.



Qili Zhao received the Ph.D. degree in control theory and control engineering from Nankai University, Tianjin, China, in 2014.

He was a Postdoctoral Researcher with Monash University, Australia, from 2014 to 2015 and with the University of Toronto, Toronto, ON, Canada, from 2015 to 2018. He is currently an Assistant Professor of College of Artificial Intelligence with Nankai University, Tianjin, China. His research interests include robotic patch clamp systems, automated drug screening, and robotic cell manipulation and measurement.